Effects of hot rolling on microstructures, wear and corrosion resistance of Mo-Ni-W P/M alloyed steels

R.H.R. Elkilani [a,*], H. Çuğ [a], M.A. Erden [b], H. Abushrenta [a], O. Albahlol [a], B. Cicek [c]

[a] Karabuk University, Department of Mechanical Engineering, Karabuk, Turkey.
hcug@karabuk.edu.tr (H.Ç.); hamzaly1988@gmail.com (H.A.); osama.bella46@gmail.com (O.A.)
[b] Karabuk University, Department of Medical Engineering, Karabuk , Turkey.
makiferden@karabuk.edu.tr (M.A.E);
[c] Hitit University, Technical Sciences Vocational School, Corum, Turkey.
cicekbunyamin78@gmail.com (B.C)
* Correspondence: rajabelkilani@gmail.com (R.H.R.E.)

(Received 04 April 2024; Accepted 22 November 2024)

ABSTRACT

This study analyzes how hot rolling changes the Fe-0.55C-3Mo-10Ni-0.5W alloy steel's microstructure, tensile strength, wear, and corrosion behaviors. Metal powders were pressed at 750 MPa pressure, and the cold-pressed samples were sintered at 5°C/min up to 1400°C for two hours in a mixed-gas environment of 90% nitrogen and 10% hydrogen. Following that, the generated steels underwent hot rolling at 40% and 80% deformation rates. The microstructures demonstrate that MoC(N), WC(N), and MoWC(N) were created and that the steels had finer microstructures and better mechanical characteristics as the deformation rate increased. As the degree of distortion increased, the wear reduced. Furthermore, the hot rolling method improved corrosion resistance, as shown by the Tafel curve analysis. The greatest factor supporting corrosion resistance was the increase in density value throughout the rolling process.

Keywords: Hot rolling, Powder Metallurgy, Characterization, Alloy steels, Wear, Corrosion.

1. INTRODUCTION

The performance of materials under varying environmental conditions is becoming increasingly critical due to advancements in science and technology. Alloyed steels are renowned for their exceptional weldability, durability, toughness, and corrosion resistance, achieved through various strengthening mechanisms and thermomechanical techniques [1]. While steels contain carbon, the addition of alloying elements such as Mo, Ni, W, Nb, Cr, and Si significantly enhances their mechanical properties [2,3].

Molybdenum and molybdate compounds are effective in improving steel's passive film stability. These compounds act as anodic corrosion inhibitors and are used in applications such as airplanes and ground vehicles due to their non-toxic nature and effective corrosion prevention [4]. Molybdate chemicals work through mechanisms of adsorption, oxidation, and deposition. Mo can also serve as a coating material for other metals, offering additional protection [5,6]. Research has shown that Mo increases steel hardness and enhances precipitation-hardening in high-strength low-alloy (HSLA) steels. Mo positively affects the microstructure and mechanical properties of steels, making them suitable for demanding applications [7–9]

Nickel (Ni) is crucial for improving steel's strength, ductility, and oxidation resistance. Ni stabilizes the ferrite phase, reduces grain size, and improves hardness and fatigue resistance,

especially when combined with chromium [10–12]. Nickel and chromium are vital in heat-resistant steels used in high-temperature applications across industries such as petrochemical, aviation, and power generation [13–15]. Tungsten (W) is another important alloying element due to its high strength, density, and melting point. Its combination with other metals enhances corrosion resistance and mechanical properties, making it suitable for high-speed engine components and tool steels [16–18].

Despite these advancements, there is limited research on Mo-Ni-W-containing alloy steels, particularly regarding how different deformation rates and cooling processes affect their microstructure and properties. This study aims to address this gap by investigating the impact of hot rolling on Mo-Ni-W alloyed steel produced via powder metallurgy. The study will involve developing various steel compositions through powder metallurgy and cold pressing, followed by hot rolling to 40% and 80% deformation. The resulting microstructures, hardness, wear, and corrosion resistance of both deformed and undeformed samples will be analyzed in detail [19–22].

Additional studies are necessary to fully understand how these alloying elements interact under different conditions. This research will provide insights into the optimal conditions for enhancing the performance of Mo-Ni-W alloyed steels, thereby contributing valuable information to the field [23–28]. The results will help in developing advanced materials for applications requiring high strength, durability, and resistance to wear and corrosion [29–33].

By exploring these aspects, the study aims to contribute to the development of more effective and reliable materials for various industrial applications [34–38]. The findings will be significant for improving the performance and longevity of components made from Mo-Ni-W alloyed steels, addressing current gaps in knowledge and practice [39–42]

Summary: This research focuses on investigating the effects of hot rolling on Mo-Ni-W alloyed steel produced via powder metallurgy. By examining various deformation rates and their impact on microstructure, hardness, wear, and corrosion resistance, the study aims to provide a comprehensive understanding of how these alloying elements perform under different conditions. The findings are expected to offer valuable insights into optimizing the properties of Mo-Ni-W steels, ultimately contributing to advancements in materials used in demanding industrial applications.

2. MATERIALS AND METHODS

In order to use the powder metallurgy technique, alloyed steel samples with the chemical composition Fe-0.55C-3Mo-10Ni-0.5W were created for this study. Table 1 lists the powders' sizes and purities. The powders were weighed to a precision of 0.0001 g using a RADWAG AS-60-220 C/2 scale, then mixed and compacted into molds before being sintered to form the final samples.

Table 1. The sizes and purities of the Powders.

	Elemental powders	size (µm)	Purity %	Supplier
1	Iron	≤180	99.9%	Höganas, USA
2	Graphite	<20	96.5%	Höganas, USA
3	Molybdenum	<150	99.9%	Aldrich, Germany
4	Nickel	<44	99.7%	Aldrich, Germany
5	Tungsten	<44	99.95%	Nanografi, Türkiye

Each Fe-0.55C-3Mo-10Ni-0.5W powder composition was generated and blended using a TUR-BULA T2F (Willy A. Bachofen AG, Muttenz, Switzerland) for many hours. It enhanced 3D motion. The particles were compressed using a 750 MPa hydraulic press (Hidroliksan, Konya, Türkiye). The samples were sintered for two hours at 5°C per minute up to 1400°C in a mixed-gas (90% nitrogen/10% hydrogen) atmosphere. After that, it was cooled to room temperature at 5°C/min.

Table 2. Chemical compositions of the PM steels.

Sample	C	Mo	Ni	W	Fe
(sample-1) Fe-0.55C-3Mo-10Ni-0.5W Undeformed	0.55	3	10	0.5	Rest
(sample-2) Fe-0.55C-3Mo-10Ni-0.5W 40% Deformed	0.55	3	10	0.5	Rest
(sample-3) Fe-0.55C-3Mo-10Ni-0.5W 80% Deformed	0.55	3	10	0.5	Rest

Sintered samples were hot-rolled using different passes. A reduction ratio of 20%, a preheating temperature of 1150°C, a holding period of 30 minutes, and ultimate rolling temperatures above 950°C were used during rolling. Samples were continuously rolled under the same rolling specifications until 40% deformation was removed to cool at room temperature, and the remaining samples were returned to the furnace for heat preservation for hot rolling after each rolling pass at 1150°C and a holding time of 30 minutes in a Protherm heat treatment furnace until 80% deformation. Then, it was also taken out to cool in the air to room temperature. The roller diameter used in the rolling process is 200mm. The number of rolling cycles is 20 cycles/minute. The hot-rolled and unrolled samples are visually distinguishable based on their surface characteristics. The material with an initial thickness of 12.32 mm was reduced to 2.76 mm through 80% cold deformation, while the sample with 40% cold deformation was reduced from 12.41 mm to 6.85 mm.

A Radwag density kit (ASTM B 328-96) (Bruker Alpha, Bursa, Türkiye) was used to determine the specimen densities (using Archimedes principle) [43]. Before examining the materials under an optical microscope, their surfaces were cleaned, abrasive papers with the different mesh sizes were used. After that, polishing with a 0.3μm Al_2O_3 suspension was done, and 1HNO_3+3HCl etching was the next. Later, ethyl alcohol and distilled water were applied to clean them all, and air drying was conducted.

An optical microscope, Nikon ECLIPSE L150 type (Melville, NY, USA), was used for the research. SEM and XRD were used to analyze the microstructural and wear-and-corrosion surface using a Zeiss microscope and a Rigaku Ultima IV diffractometer. XRD was used to qualitatively analyze the structural changes in alloys after adding Mo, Ni, and W.

A (HMV-Shimadzu, Tokyo, Japan) micro hardness tester was employed under an HV0.5 load for a duration of 15 seconds. The hardness value was calculated by averaging five hardness tests from each sample.

Before the corrosion test, copper wire was soldered to the samples to ensure the conductivity of the samples with the corrosion unit. Then, they were molded with epoxy resin to provide insulation. Additionally, ethyl alcohol was used to clean the surface after abrasive papers with different mesh sizes up to 1200 were used. On the surface of the specimen, a thick adhesive tape was applied with a hole of 0.25 cm in diameter. In order to avoid any potential negative consequences, the corrosion tests were conducted on all specimens in the same location. Potentiodynamic polarization tests were done at room temperature in 3.5% NaCl utilizing a Gamry model PC4/300mA potentiostat/galvanostat with computer-controlled DC105 corrosion analysis. A three-electrode electrochemical cell was used for the corrosion tests, with graphite as the counter electrode and a saturated calomel electrode as the reference electrode. In this setup, a classic corrosion cell configuration was employed, where the working (sample) electrode, counter electrode, and calomel electrode were positioned in close proximity to one another.

Samples for the wear test were prepared using 400, 600, 800, 1000, 1500, 2000, and 2500 meshes of coarse-to-fine abrasive paper. The 4D-ECN (in Türkiye) tribometer was used for wear tests. The dry wear test was performed at room temperature with 20N and 40N loads, a 10mm stroke, 100 meters of sliding distance per load, and 0.04 m/s sliding speed. For the wear test, AISI 52100 6mm

chrome steel balls were used. A profilometer (Mitutoyo SJ-410, Tokyo, Japan) was used to measure the alloy steel surface's wear markings after the wear test. Then, wear-line SEM pictures were taken.

3. RESULTS AND DISCUSSIONS

Fig. 1. illustrates the microstructure of undeformed Mo-Ni-W steel, In Fig. 1, it was observed that bainite, martensite, and austenite, were formed in the microstructure.

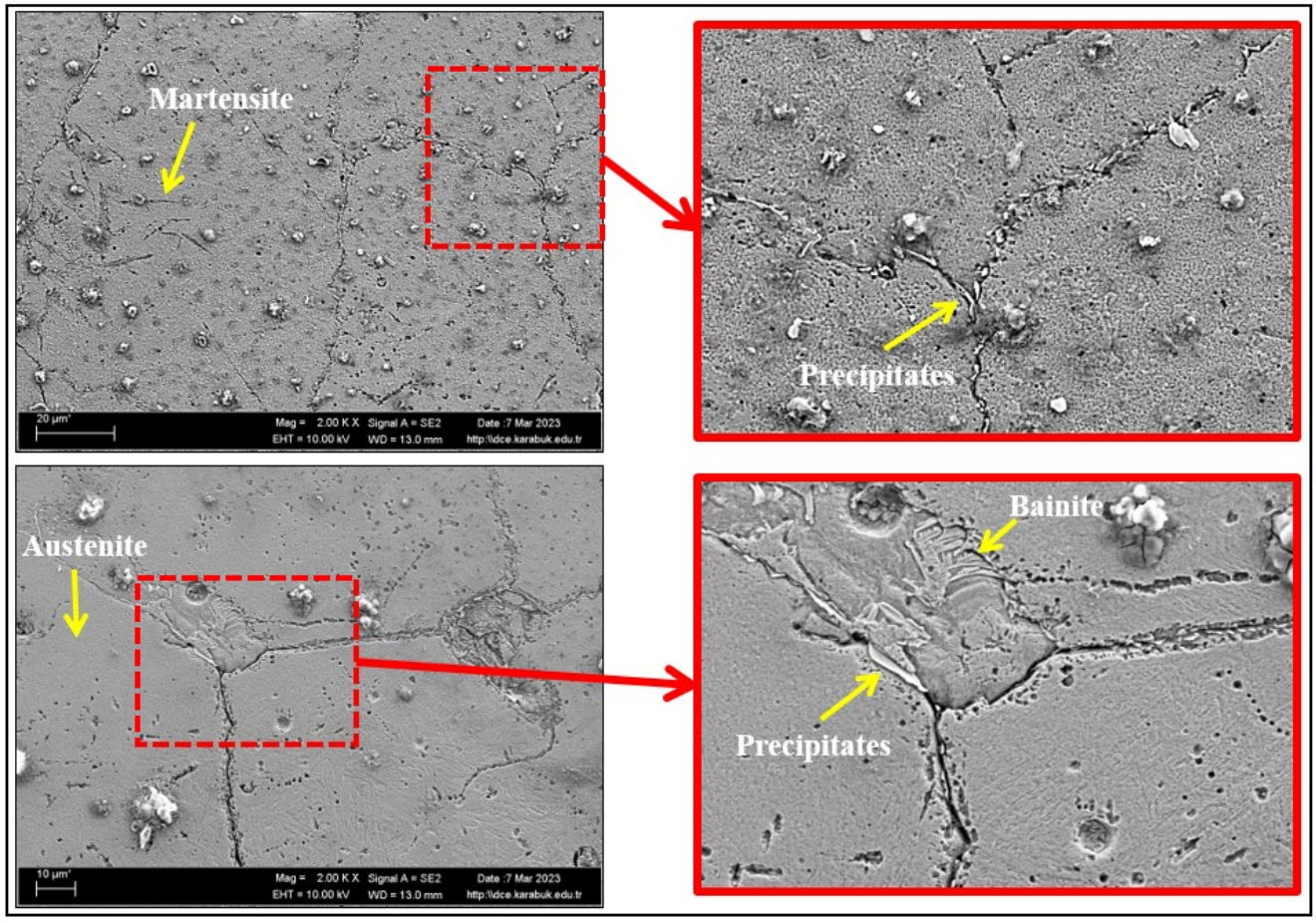

Fig. 1. Microstructure details for undeformed sample (2000x-5000x).

Furthermore, Fig. 2. illustrates how the grain size reduces with increasing deformation. It was discovered that the addition of Mo and W reduces the grain size. The production of MoC(N), WC(N), and MoWC(N) precipitates in grains and grain borders might cause grain refining [44,45]. On the other hand, many studies in the literature show that deformation refines the grain size [41,46–48]. For instance, according to Inagaki [47], ferrite nucleation and subsequent grain refinement are enhanced by adding highly stressed patches at grain borders or close to the boundaries of annealing twins. It suggests that the deformation in the non-recrystallizing zone of austenite accelerates the nucleation rate and ferrite formation. Little ferrite particles are created as a result, and the structure's ferrite volume rises [48]. In addition, the results obtained from this study showed that 80% of deformed samples exhibited smaller grains than sintered materials. Li [46] investigated how the forging rate affected the microstructure of H13 steel and found that as the forging rate increases, grain size reduces, providing more nucleation points and storing energy for grain recovery and recrystallization.

Therefore, it has been observed that it promotes grain thinning.

Fig. 2 presents SEM point EDS analysis and mapping images of 40% deformed samples, while Fig. 3 shows the same for 80% deformed samples. Microstructural analysis revealed that heat deformation reduced pores and grain size. Solution-based alloying had little impact on austenite recrystallization, while precipitated particles strongly inhibited grain boundary movement [49]. Hong et al. investigated the effects of tungsten addition to 9Cr–Mo steels (M10, W18, W27) on microstructure and high-temperature tensile strength. Tungsten improved tensile strength by increasing the Cr/Fe ratio, which led to lattice expansion and dislocation glide pinning. M23C6 carbides were fine and homogenous in tungsten-treated 9Cr steels, while they agglomerated in M10 steel. The high tensile strength of tungsten-added 9Cr steels was attributed to stable M2X and M23C6 carbides and reduced iron self-diffusivity after tempering, which hindered dislocation recovery.

Adding W to 9Cr steels has been shown to delay phase transformation processes and stabilize their microstructure. The incorporation of tungsten in these steels results in the formation of M2X carbonitrides and homogeneous M23C6 carbides, alongside the retarded dislocation recovery, thus improving the material's mechanical properties [50]. As shown in Figs. 3 and 4, EDS analysis of both sintered and 80% deformed materials reveals the presence of precipitates in various sizes, including Fe3C, MoC, MoC(N), WC, and WN. These precipitates form due to the interactions between Fe, C, Mo, and W elements. The EDS results further indicate that deformation accumulation plays a crucial role in initiating the precipitation of carbonitrides in steels, a phenomenon that is influenced by the alloying elements such as Mo and W, which enhance precipitation during deformation [51,52].

Fig. 3 illustrates SEM images, including line EDS and point EDS analysis of precipitates formed within the grains and at grain boundaries, along with mapping images of Mo and W in the 80% deformed steel. EDS analysis results from this work, and prior studies show that alloyed PM steels can include MoC(N) and WC precipitates. Microscopic precipitates such as MoC, WC, MoN, WCN, MoCN, and WMoCN may form during 1400°C sintering or post-sintering cooling. EDS showed Mo and W precipitated as grains/grain boundaries (Fig. 3). The EDS line analysis showed that the alloy comprised a diversity of components in both kind and quantity along the matrix-precipitate line (Fig. 3). Mo is abundant in the spherical precipitate. In contrast, iron is abundant in the matrix phase. The concentration of Mo increases significantly when the analytical line and the precipitates converge. The PM steel samples have precipitates (confirmed by SEM and EDS studies) that are known to substantially affect austenite recrystallization and grain development [9,12].

Small ferrite grains are created when precipitates that do not dissolve at the sintering temperature stop the growth of austenite grains [31,53–55].

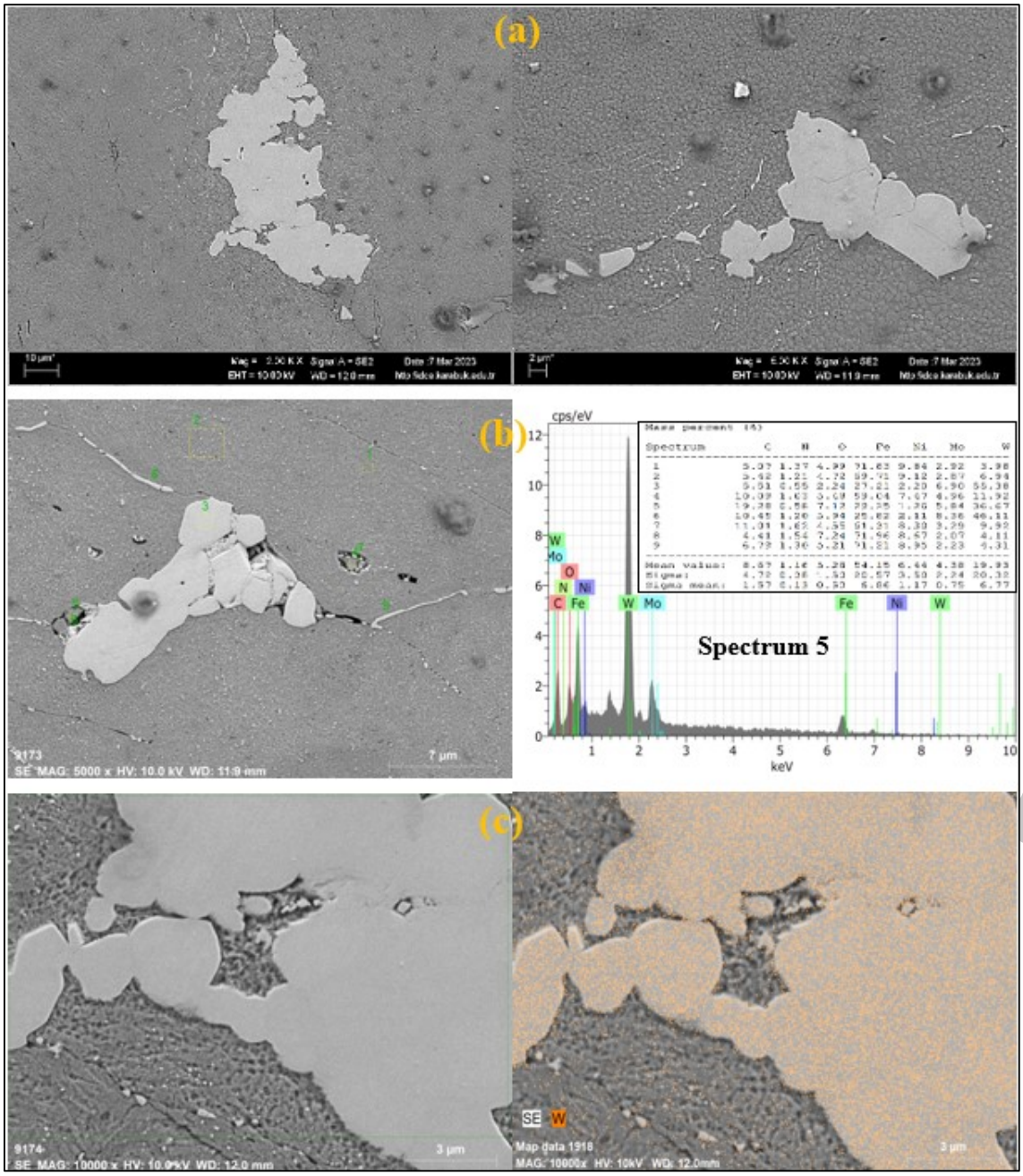

Fig. 2. Mo-Ni-W steel 40% Deformed (a) SEM Microstructure images (2000x-5000x), (b) SEM point EDS analysis (5000x), (c) SEM mapping images (10000x).

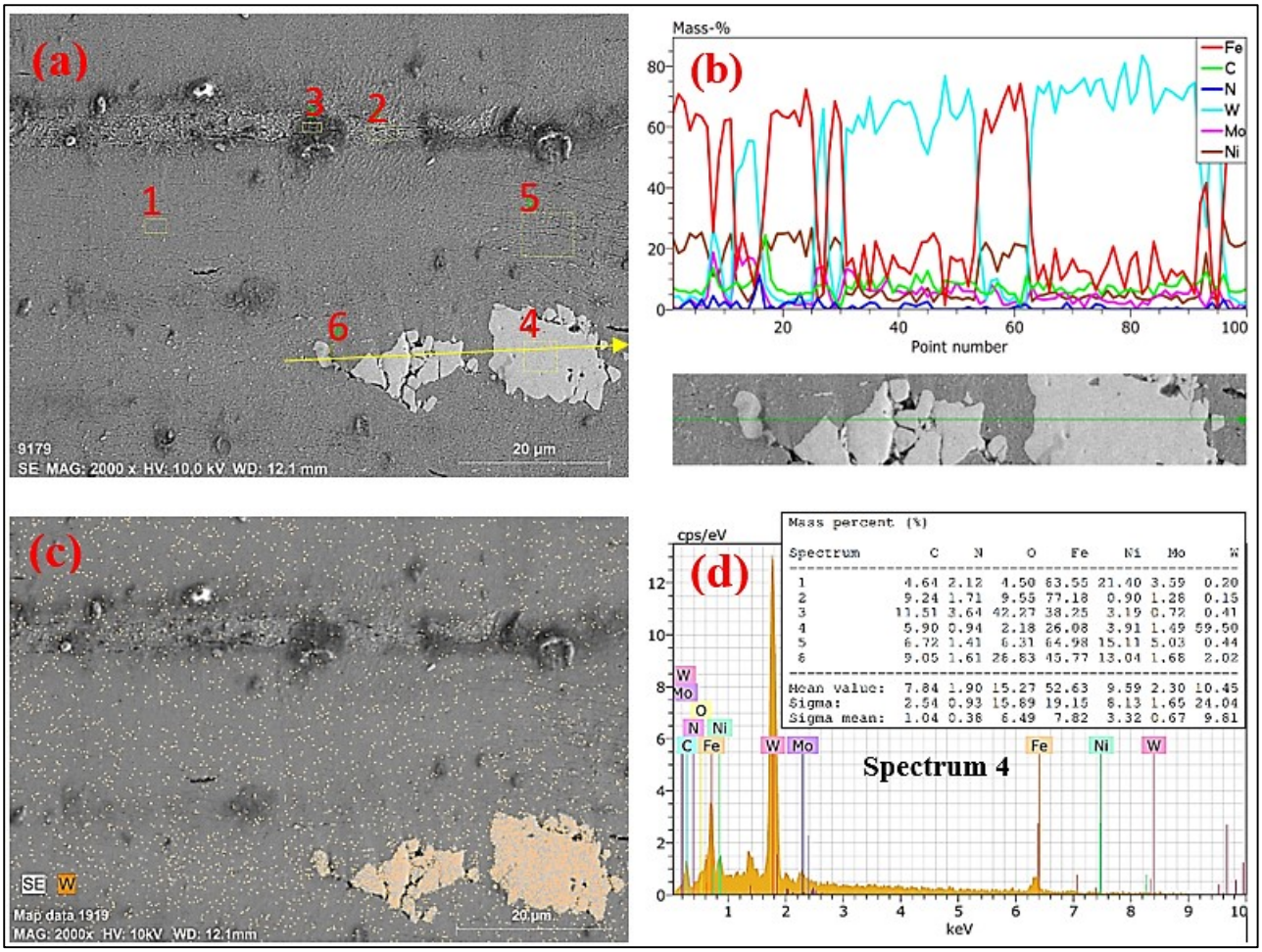

Fig. 3. Mo-Ni-W steel 80% Deformed (a, b, and d) SEM point EDS images, and line EDS analysis (2000x), (c) SEM mapping images (2000x).

The SEM microstructure and EDS results obtained from Mo-Ni steel after deformation (Fig. 3 and Fig. 4) reveal the formation of nano-sized precipitates on both the grain and grain boundaries, consistent with previous studies [56]. These precipitates, primarily composed of Mo, contribute to the stabilization of the microstructure. Tracey [50] and Reyes et al. [51] observed bainite and martensite phase formation in similar steels, while Alharthi [52] showed that the transformation to bainitic structures is facilitated by C and Mo, even in the absence of Ni in the Fe particle center. EDS analysis indicates the presence of Ni-rich austenitic regions, which transform into martensite over time, with longer sintering times increasing the amount of Ni-rich martensite. Additionally, Fig. 4 highlights martensite phase formation, with Mo playing a key role in preventing grain growth by forming precipitates such as MoC, MoN, and MoCN, as supported by [55,60,61]. These findings underline the significant role of Mo and Ni in phase formation and microstructural stabilization, aligning with previous research.

Fig. 5. XRD shows the patterns of Mo-Ni-W steel. Depending on the alloy type, XRD patterns and predictions about which compounds may have formed in the pattern peaks are shown in Fig. 5. Considering the XRD pattern of Fe+0.55C+3Mo+10Ni+0.5W alloy, where all elements and compounds are seen together, it is approximately 38° for the MoN compound, 44° for Fe_3Ni_2, and WMoC compounds, 48° for WN compound, 68° for MoWCN compound, 76° for WMoC compound and 82° for WC compound.

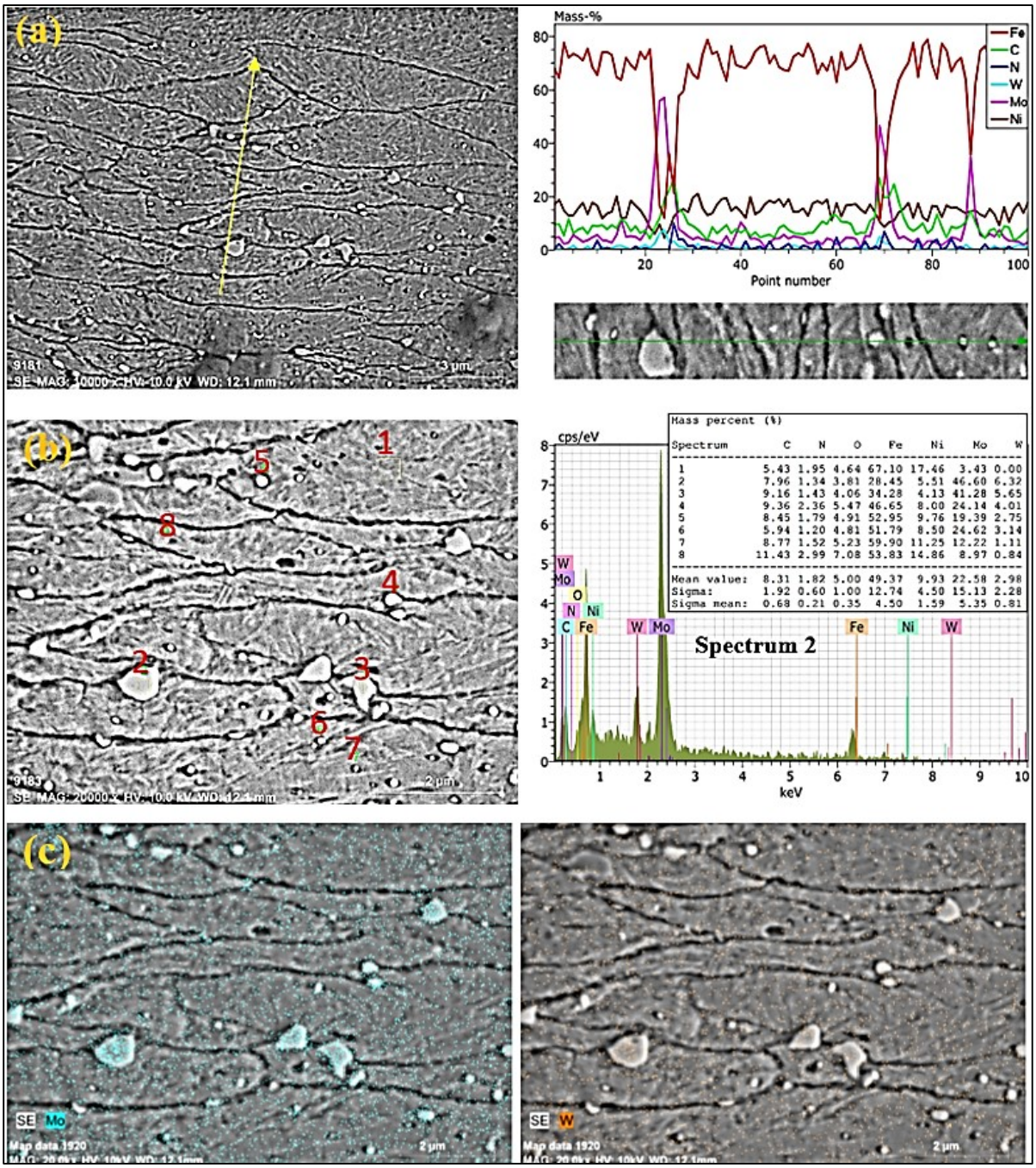

Fig. 4. Mo-Ni-W steel 80% Deformed (**a**) SEM. Line EDS images (10000x), (**b**) SEM point EDS analysis of precipitates formed in the grain and grain boundaries (20000x), and (c) mapping images of Mo and W.

Hardness test results indicate that the hardness values of Mo-Ni-W steels increased as the rate of deformation increased. Specifically, the hardness values of Mo-Ni-W steel were 283.8 Hv for sintered, 378.6 Hv for homogenized, 40% deformed, and 573 Hv for 80% deformed samples, respectively.

The increased number of precipitates that form in alloyed steel, such as MoN, MoC, WC, and WN, as well as the grain refinement that occurs in steel with a rising deformation rate, are both responsible for this rise in hardness. The production of these precipitates was verified by the XRD data. In contrast to undeformed steel,

alloyed steel had a harder grain structure and reduced grain size due to precipitates that hindered grain growth and dislocation movement. The impact of alloy elements on grain boundary movement and recrystallization is due to precipitates of carbonitride that either developed during cooling or remained undissolved in austenite. Furthermore, as plastic deformation (strain-induced precipitation) increases, so does the rate of precipitation. Grain diameters were reduced, and strength increased when precipitated particles prevented grain boundary movement [62,63]. Earlier micro hardness studies [64,65] on ferrite grains revealed that precipitation hardening is primarily responsible for the micro-alloyed steels' increased hardness.

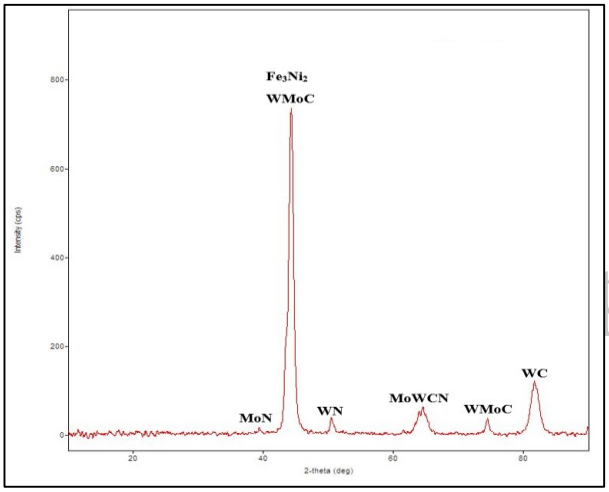

Fig. 5. XRD patterns of Mo-Ni-W steel.

Changes in density and porosity were noted in addition to precipitates and refinement of grain size. A few factors influence the porosity of powder metallurgy steels. They include deformation rate, alloying, sintering temperature and duration, and pressing methods (e.g., warm, hot, and cold). In general, alloying makes porosity higher [66]. However, sintering time and temperature reduce porosity [66,67]. The relative densities (%) of the alloyed and unalloyed steels are displayed in Table 3. It is found that when the deformation rate increases, both steels' relative densities increase, and the porosity percentage decreases in tandem. It is thought that the porosity level of specimens made via powder metallurgy also has an impact on their hardness values. Pores can contribute to the propagation of fractures if their shape is not aligned, as they can function as a stress raiser and start cracks where stress is concentrated [68]. It was found that as deformation rates increase, the amount of porosity decreases. Steels that were alloyed became harder as a result.

Tastemur et al. [68] have investigated the 40% and 75% thickness reduction processes used to manufacture powder metallurgy-produced unalloyed steel and micro-alloyed steel with 0.15% Nb. They discovered that in both steels, the grain size progressively shrank with the rate of deformation. The grain size study corroborated that tiny grains resulted from a full recrystallization process at a 75% deformation rate. The increase in deformation rate resulted in a rise in the density and hardness values. Under sintered conditions, the micro-alloyed steel's density and hardness were 89.46% and 75 HV, respectively. However, in a 75% deformed state, those same values were 98.51% and 231 HV.

Table 3. Density and porosity of samples.

Alloys	Experimental Densities (g/cm3)	Porosity (%)
(sample-1) Undeformed	6.9948	13.38
(sample-2) 40% Deformed	7.4762	7.42
(sample-3) 80% Deformed	7.8957	2.22

The wear depth results for all samples under a 40N load indicate the impact of applied load on wear depth. It was observed that as the degree of deformation increased, the wear depth decreased. The lowest wear track depth was found in the sample with 80% deformation, while the highest depth was observed in the sample without deformation. According to morphology obtained from the surface roughness device, the undeformed sample exhibited adhesive wear, whereas the 80% deformed sample showed abrasive wear. This suggests that increased deformation significantly enhances wear resistance, reducing surface wear.

The wear test and volume loss results of the samples reveal that, similar to the area loss findings, the volume loss decreases with increasing deformation. Specifically, the undeformed sample exhibited a volume loss of 2.58 mm^3 under a 20N load and 3.12 mm^3 under a 40N load. In contrast, the sample with 40% deformation showed a reduced volume loss of 1.1 mm^3 at 20N and 1.99 mm^3 at 40N. The sample with 80% deformation experienced the lowest volume losses, with only 0.5 mm^3 under 20N and 0.9 mm^3 under 40N. These results suggest that higher deformation levels significantly improve wear resistance, as seen in the consistently lower volume losses at both load levels for more deformed samples.

The average friction coefficient values observed during the wear test show a decrease as the level of deformation increases. For the undeformed sample, the friction coefficient was 0.79 under a 20N load and decreased slightly to 0.69 under a 40N load. In comparison, the sample with 40% deformation exhibited reduced friction coefficients of 0.55 at 20N and 0.50 at 40N. The sample with 80% deformation recorded the lowest friction coefficients, with values of 0.43 under 20N and 0.49 under 40N. This trend suggests that increased rolling deformation leads to a smoother surface and enhanced contact stability, likely due to a more compact and refined microstructure, ultimately lowering the friction coefficient. Erden and Aydin [69] mentioned that they successfully used powder metallurgy to create AISI 8620 steel, which they then carburized for four hours at 925°C. They discovered that as carburization proceeds, the average friction coefficient tends to decrease. An analysis of worn surfaces revealed the presence of oxidative wear at 15 N of load. At greater loads, oxidative wear transforms into abrasive wear. An investigation was conducted by Zhou et al. to determine how the microstructural development of carburized G20CrNi2MoA-bearing steel was influenced by the surface friction characteristics and the complete forming process [70].

The wear rate significantly decreased as hot rolling distortion increased, with a quick early wear period followed by a stable wear stage. The friction coefficient also decreased with hot rolling deformation, dropping by 45% compared to the raw material, and 50% in total [71,72]. High friction, especially in dry conditions, causes material accumulation and cracks. AISI 52100 chrome steel balls accumulate on the workpiece surface under high friction or dry conditions, with material deposition visible only in dry environments [73,74].

Fig. 6. illustrates the worn surface images of all samples subjected to both 20N and 40N loads, providing a detailed view of the wear patterns and surface damage that occurred under varying loading conditions.

t

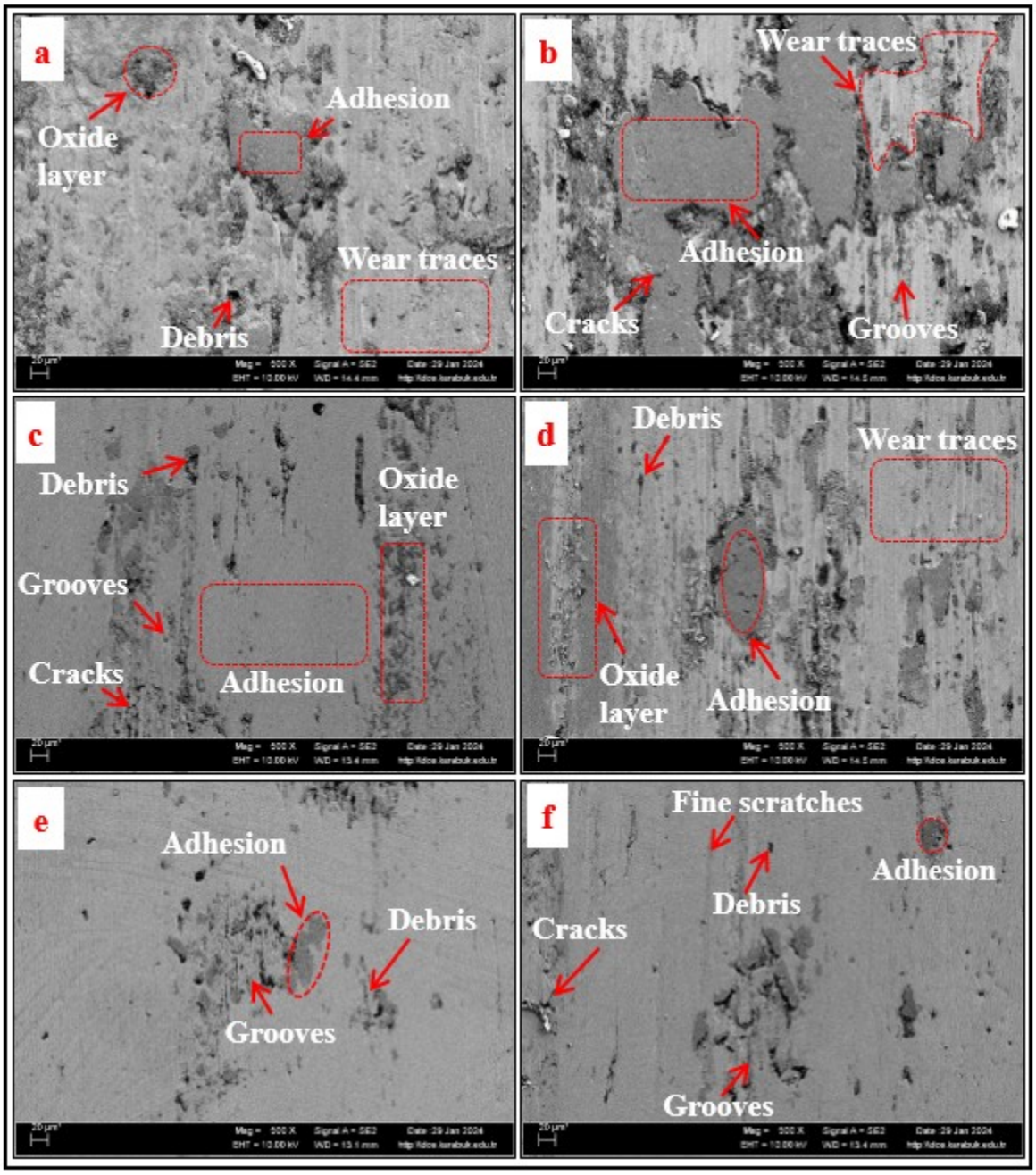

Fig. 6. Worn surface images of alloys: a) undeformed 20N, b) undeformed 40N, c) 40% Deformed 20N, d) 40% Deformed (40N), e) 80% Deformed (20N), and f) 80% Deformed (40N).

Dry sliding wear tests remove components from contact surfaces, causing abrasive wear, while others accumulate in wear channels, fracture, and deform the surface. Powdered metal steel samples lost material through various wear mechanisms, as shown by surface morphological changes. At low weights (20 N), scuffing, cracks, and potholes appeared. Friction force pressed worn debris into the surface, causing material loss and fractures. Frictional heat caused material to adhere between the ball and workpiece at high loads, favoring shedding and adhesion in dry conditions.

Fig. 7. shows SEM images and EDX results of the worn surface of all samples under 20N and 40N load. Small pits were also observed forming in the wear SEM images, as shown in Figs. Powdered metal's strain-hardening properties

boost steel's wear resistance, and wear debris cuts through the substrate and creates microscopic grooves. During wear testing, sliding friction heats the powder metal steel surface, reacting with air oxygen to produce substantial oxide.

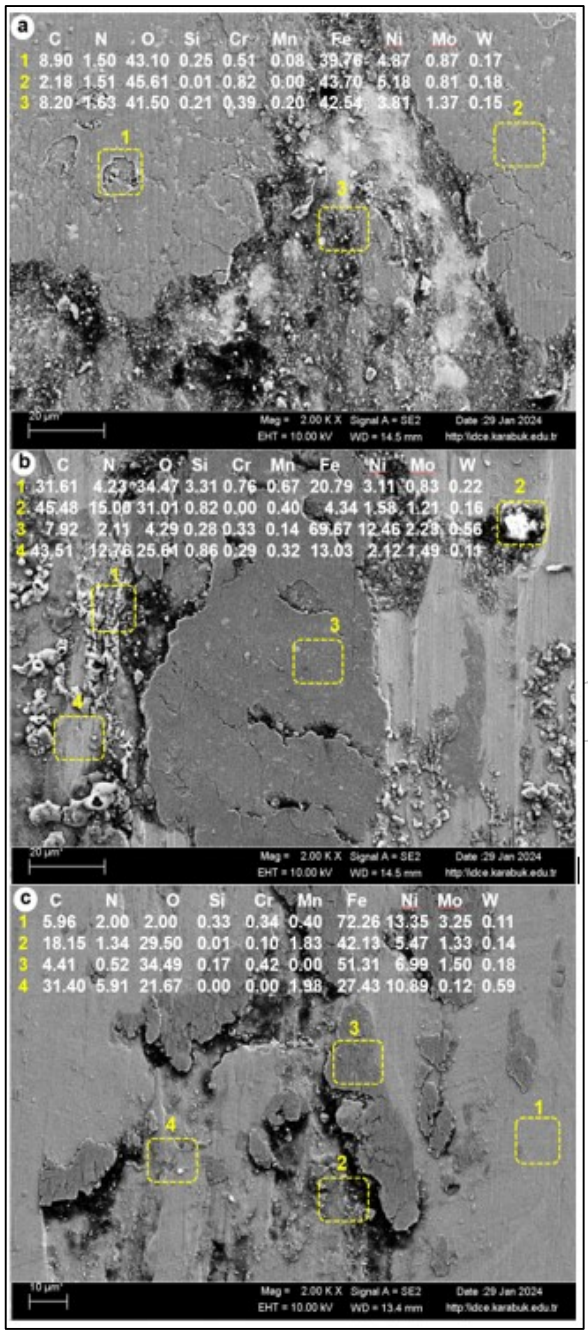

Fig. 7. SEM images and EDX results of the worn surface under 40N load: a) Undeformed samples, b) 40% deformed, and c) 80% deformed samples.

The profile images of abrasive balls used in wear tests under 40N load show the effect of counter material hardness on surface profile. High-precision AISI 52100 chrome steel balls were used. The ball against the 80% deformed sample, which had the highest hardness, exhibited a rougher surface. For the undeformed sample, the wear mark depth was 40 microns, width 0.95 microns, indicating adhesive wear. The 40% deformed sample's ball showed a depth of 57 microns and width 1.05 microns, with mainly adhesive wear but abrasive characteristics in deeper areas. The ball opposite the 80% deformed sample had a depth of 48 microns and width 1.25 microns, with almost entirely abrasive wear.

Fig. 8. Shows the SEM and EDX analysis of abrasive balls of the test carried out at 40N load. The test findings showed that the balls were abrasive and sticky depending on the load. EDS analysis of the ball revealed a sticky coating, proving an adhesive mechanism. The ball surface EDX research results are displayed in Fig. 8 [75].

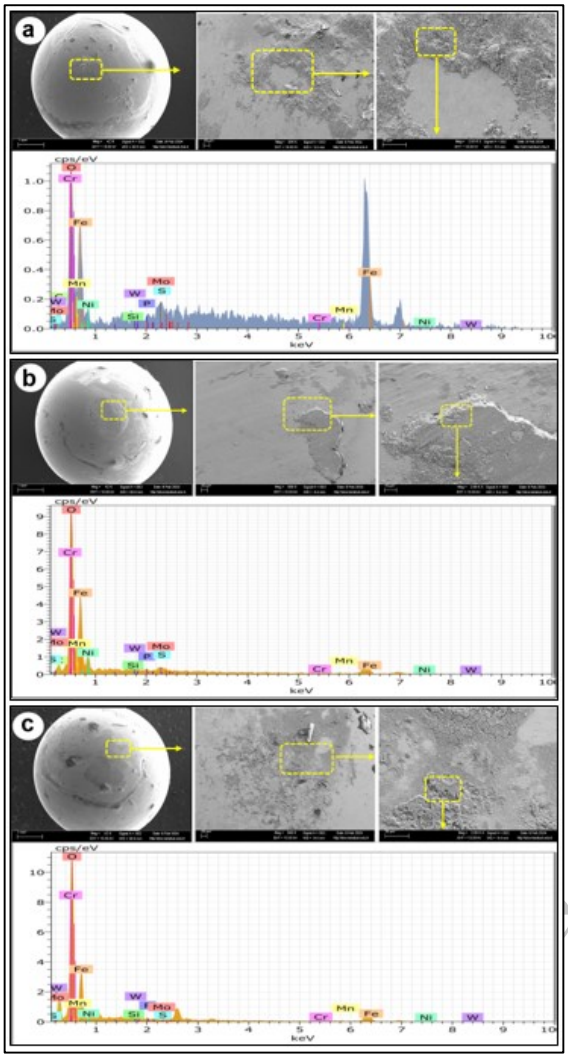

Fig. 8. SEM and EDX analysis of abrasive balls of the test carried out at 40N load: a) Undeformed, b) 40% deformed, and c) 80% deformed.

The potentiodynamic polarization curves of the samples indicate their electrochemical behavior. Table 4 presents the corrosion potentials (Ecorr), current densities (Icorr), and corrosion rates (CR). Increased deformation raised corrosion potential and reduced corrosion current density, suggesting improved corrosion resistance. The correlation between lower corrosion rate, higher corrosion potential, and lower current density is significant [76], as pitting corrosion is more active in samples with lower current density [77]. This is attributed to the galvanic effect in the undeformed sample, with coarser grains and fewer grain boundaries, promoting pit formation [78]. The surface images after corrosion are shown in Figure 9, illustrating the formation of iron oxide and hydrochloric acid during the corrosion process, which deepens pits and accelerates rusting [79].

Table 4. Ecorr, Icorr, and corrosion rate values of the alloys.

Alloys	Ecorr (mV)	Icorr ($\mu A/cm^2$)	Corrosion rate (mm/year)
(sample-1) Undeformed	-174.0	37.4	0.753
(sample-2) 40% Deformed	-127.0	33.4	0.68
(sample-3) 80% Deformed	-96.9	29.1	0.482

$$Fe^{+2} + 2NaCl + 2OH^- \rightarrow FeCl_2 + 2NaOH \quad (1)$$

$$FeCl_2 + (1/4)O_2 + (5/2)H_2O \rightarrow Fe(OH)_3(s) + 2HCl \quad (2)$$

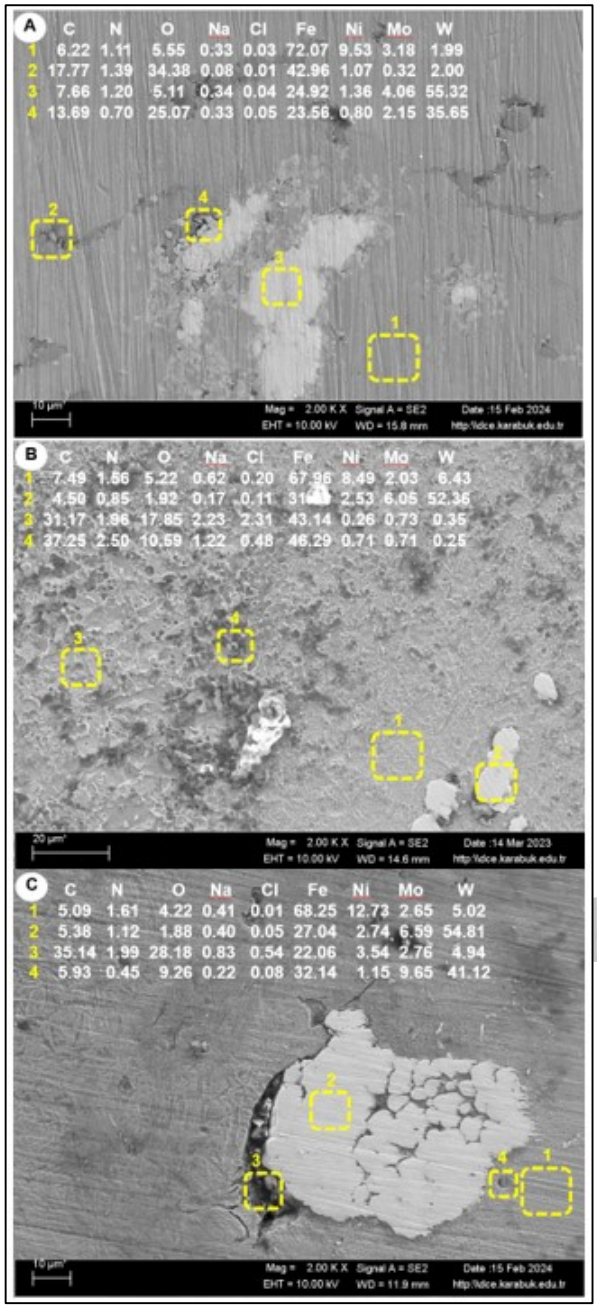

Fig. 9. SEM images and SEM EDX results of the samples after the corrosion test a) 40% Undeformed, b) 40% Deformed, and c) 80% Deformed.

CONCLUSION

The Fe-0.55C-3Mo-10Ni-0.5W composition was produced by powder metallurgy and deformed at 40% and 80% by hot rolling. The study concluded:

1. The microstructure includes martensite, pearlite, austenite, and residual austenite phases. Ni enhances martensite and bainite, while Mo promotes pearlite and bainite.
2. Deformed PM steels show better mechanical properties, finer microstructure, reduced grain size, porosity, and increased density and precipitate formation (MoC(N), WC(N), MoWC(N)).
3. EDS analysis revealed Fe, C, N, Mo, Ni, and W in the iron matrices, with XRD confirming compounds like Fe3Ni2, WMoC, WN, and WC.
4. Hardness increased with deformation due to precipitate formation and grain refinement.
5. Wear depth was lowest at 80% deformation and highest in the undeformed sample. Wear depth, volume loss, and friction coefficient decreased with increased deformation.
6. Higher deformation reduced polarization resistance, likely due to increased density and finer grain size. Mo, Ni, and W contribute to corrosion resistance by forming passive films.
7. The study shows decreasing wear depth and friction with higher deformation. Further exploration of deformation ratios and load conditions is needed.
8. The research highlights dry sliding wear's impact on material loss. Future studies should assess wear in lubricated or humid environments for real-world applications.

Funding: This research received no external funding.

Acknowledgments: This study was carried out as a part of Ph.D. thesis by “Rajab Hussein Rajab Elkilani” at the Institute of Graduate Studies, Karabuk University, Karabuk, Turkey.

Conflicts of Interest: “The authors declare no conflict of interest.”

REFERENCES

[1] S. Gündüz, H. Karabulut, M.A. Erden, M. Türkmen, Microstructural effects on fatigue behaviour of a forged medium carbon microalloyed steel, Materialpruefung/Materials Testing, 55 (2013) 865–870. https://doi.org/10.3139/120.110511.

[2] B. Kianian, Comparing acquisition and operation life cycle costs of powder metallurgy and conventional wrought steel gear manufacturing techniques, Proceedings of the CIRP, Elsevier, 2019, pp. 1101–1106. https://doi.org/10.1016/j.procir.2019.03.260.

[3] A. Flodin, Powder metallurgy technology: A review of the state of the art, Power Transmission Engineering, 2016, 38–43.

[4] L.B. Coelho, E. Fava, A.M. Kooijman, Y. Gonzalez-Garcia, M.-G. Olivier, Molybdate as corrosion inhibitor for hot dip galvanised steel scribed to the substrate: A study based on global and localised electrochemical approaches, Corrosion Science, 175 (2020) 108893. https://doi.org/10.1016/j.corsci.2020.108893.

[5] M. Wu, H. Ma, J. Shi, Beneficial and detrimental effects of molybdate as an inhibitor on reinforcing steels in saturated Ca(OH)2 solution: Spontaneous passivation, Cement and Concrete Composites, 116 (2021) 103887. https://doi.org/10.1016/j.cemconcomp.2020.103887.

[6] M. Wu, J. Shi, Beneficial and detrimental impacts of molybdate on corrosion resistance of steels in alkaline concrete pore solution with high chloride contamination, Corrosion Science, 183 (2021) 109326. https://doi.org/10.1016/j.corsci.2021.109326.

[7] H. Halfa, Thermodynamic Calculation for silicon modified AISI M2 high speed tool steel, Journal of Minerals and Materials Characterization and Engineering, 01 (2013) 257–270. https://doi.org/10.4236/jmmce.2013.15040.

[8] W.B. Lee, S.G. Hong, C.G. Park, K.H. Kim, S.H. Park, Influence of Mo on precipitation hardening in hot rolled HSLA steels containing Nb, Scripta Materialia, 43 (2000) 319–324. https://doi.org/10.1016/S1359-6462(00)00411-5.

[9] K. Junhua, Z. Lin, G. Bin, L. Pinghe, W. Aihua, X. Changsheng, Influence of Mo content on microstructure and mechanical properties of high strength pipeline steel, Materials and Design, 25 (2004) 723–728. https://doi.org/10.1016/j.matdes.2004.03.009.

[10] C.U. Steels, metals The Effect of Electroslag Remelting on the Microstructure and Mechanical Properties of, (2020) 1–9.

[11] G. Pavapootanont, P. Wongpanya, E. Viyanit, G. Lothongkum, Corrosion behavior of Ni steels in aerated 3.5-wt.% NaCl solution at 25°C by potentiodynamic method, Engineering Journal, 22 (2018) 1–12. https://doi.org/10.4186/ej.2018.22.4.1.

[12] R. Elkilani, H. Çuğ, A. Erden, The effects of hot rolling process on mechanical properties, corrosion resistance, and microstructures of Mo-Ni alloyed steels produced by powder metallurgy, Science of Sintering, (2024) 59–78. https://doi.org/10.2298/sos230625040e.

[13] M. Fujikura, A. Kasama, R. Tanaka, S. Hanada, Effect of alloy chemistry on the high temperature strengths and room temperature fracture toughness of advanced Nb-based alloys, Materials Transactions, 45 (2004) 493–501. https://doi.org/10.2320/matertrans.45.493.

[14] J.S. Park, K.A. Lee, C.S. Lee, Effect of W-addition on low cycle fatigue behavior of high Cr ferritic steels, Metals and Materials International, 5 (1999) 559–562. https://doi.org/10.1007/BF03026305.

[15] F. Masuyama, History of power plants and progress in heat resistant steels, ISIJ International, 41 (2001) 612–625. https://doi.org/10.2355/isijinternational.41.612.

[16] T. Weber, J. Aktaa, Numerical assessment of functionally graded tungsten/steel joints for divertor applications, Fusion Engineering and Design, 86 (2011) 220–226. https://doi.org/10.1016/j.fusengdes.2010.12.084.

[17] Y. Ma, W. Zhu, Q. Cai, W. Liu, X. Pang, Microstructural evolution and mechanical properties in the partial transient liquid phase diffusion bonding of tungsten to steel, International Journal of Refractory Metals and Hard Materials, 73 (2018) 91–98. https://doi.org/10.1016/j.ijrmhm.2018.02.002.

[18] C. Lu, Y. Wang, X. Lei, J. Yang, J. Huang, S. Chen, Y. Zhao, Influence of Fe-W intermetallic compound on fracture behavior of Steel/Tungsten HIP diffusion bonding joint: Experimental investigation and first-principles calculation, Journal of Manufacturing Processes, 55 (2020) 131–142. https://doi.org/10.1016/j.jmapro.2020.03.054.

[19] W. Zhu, W. Liu, Y. Ma, Q. Cai, J. Wang, Y. Duan, Microstructural characteristics, mechanical properties and interfacial formation mechanism of tungsten alloy/steel composite structure fabricated by HIP co-sintering, Materials and Design, 211 (2021) 110127. https://doi.org/10.1016/j.matdes.2021.110127.

[20] M.A.M. Ahssi, M.A. Erden, M. Acarer, H. Çuğ, The effect of nickel on the microstructure, mechanical properties and corrosion properties of niobium-vanadium microalloyed powder metallurgy steels, Materials, 13 (2020) 4021. https://doi.org/10.3390/ma13184021.

[21] M. Jahazi, B. Eghbali, The influence of hot forging conditions on the microstructure and mechanical properties of two microalloyed steels, in: J. Mater. Process. Technol., Elsevier, 2001: pp. 594–598. https://doi.org/10.1016/S0924-0136(01)00599-4.

[22] B. Güney, Corrosion and wear behaviour of HVOF spraying WC-12% Ni coating on gray cast-iron, Indian Journal of Engineering and Materials Sciences, 28 (2021) 73–81. https://doi.org/10.56042/ijems.v28i1.34970.

[23] R.A. Phillips, J.E. King, J.R. Moon, Fracture toughness of some high density PM steels, Powder Metallurgy, 43 (2000) 43–48. https://doi.org/10.1179/pom.2000.43.1.43.

[24] J.J. Lian, X.G. Ma, Z.Y. Jiang, C.S. Lee, J.W. Zhao, A review of the effect of tungsten alloying on the microstructure and properties of steels, Tungsten, 5 (2023) 440–466. https://doi.org/10.1007/S42864-022-00174-1/TABLES/4.

[25] G. Yao, S. Pan, J. Yuan, Z. Guan, X. Li, A novel process for manufacturing copper with size-controlled in-situ tungsten nanoparticles by casting, Journal of Materials Processing Technology, 296 (2021). https://doi.org/10.1016/j.jmatprotec.2021.117187.

[26] T. Han, C. Hou, Z. Zhao, X. Huang, F. Tang, Y. Li, X. Song, W–Cu composites with excellent comprehensive properties, Composites Part B: Engineering, 233 (2022). https://doi.org/10.1016/j.compositesb.2022.109664.

[27] S. Higashino, M. Miyake, T. Ikenoue, T. Hirato, Formation of a photocatalytic WO3 surface layer on electrodeposited Al–W alloy coatings by selective dissolution and heat treatment, Scientific Reports, 9 (2019). https://doi.org/10.1038/s41598-019-52178-6.

[28] B.A. Gething, D.F. Heaney, D.A. Koss, T.J. Mueller, The effect of nickel on the mechanical behavior of molybdenum P/M steels, Materials Science and Engineering: *A*, 390 (2005) 19–26. https://doi.org/10.1016/j.msea.2004.05.087.

[29] J. Zhao, Z. Jiang, C.S. Lee, Functions of tungsten alloying in microalloyed steels, 2014. https://ro.uow.edu.au/eispapers/2909/ (accessed February 29, 2024).

[30] C.R. Sohar, Lifetime Controlling Defects in Tool Steels, 2011. https://doi.org/10.1007/978-3-642-21646-6.

[31] H. Simsir, Y. Akgul, M.A. Erden, Hydrothermal carbon effect on iron matrix composites produced by powder metallurgy, Materials Chemistry and Physics, 242 (2020) 122557. https://doi.org/10.1016/j.matchemphys.2019.122557.

[32] R. M'Saoubi, T. Czotscher, O. Andersson, D. Meyer, Machinability of powder metallurgy steels using PcBN inserts, in: Procedia CIRP, Elsevier, 2014: pp. 83–88. https://doi.org/10.1016/j.procir.2014.03.094.

[33] W. Jing, W. Yisan, D. Yichao, Reaction synthesis of Fe-(Ti,V)C composites, Journal of Materials Processing Technology , 197 (2008) 54–58. https://doi.org/10.1016/j.jmatprotec.2007.06.016.

[34] F. Okay, S. Islak, Microstructure and mechanical properties of aluminium matrix boron carbide and carbon nanofiber reinforced hybrid composites, Science of Sintering , 54 (2022) 125–138. https://doi.org/10.2298/SOS2202125O.

[35] N. Kati, S. Ozan, T. Yildiz, A. Korkmaz, controlling of the structural characteristics of ZnO nanomaterials by reaction pressure and reaction time, Science of Sintering , 54 (2022) 73–80. https://doi.org/10.2298/SOS2201073K.

[36] U. Caligulu, H. Durmus, M. Akkas, B. Sahin, Microstructure and Mechanical properties of ni matrix B4C reinforced functionally graded composites, Science of Sintering , 53 (2021) 475–484. https://doi.org/10.2298/SOS2104475C.

[37] E. Avşar, N. Durlu, A. Ataş, C. Bozacı, H. Özdural, Joining of iron based powder metallurgy parts with sintering, (2010). https://gcris.etu.edu.tr/handle/20.500.11851/6956 (accessed April 28, 2023).

[38] Y.A. M. Aydın, M. Gavas, M. Yaşar, Production Methods and Manufacturing Technologies, (2011).

[39] P. Uranga, J.M. Rodríguez-Ibabe, Thermomechanical processing of steels, Metals, 10 (2020) 248. https://doi.org/10.3390/met10050641.

[40] M.F. Ertenli, E. Erdal, A. Buyukkaragoz, I. Kalkan, C. Aksoylu, Y.O. Özkılıç, Lateral torsional buckling of doubly-symmetric steel cellular I-Beams, Steel and Composite Structures, 46 (2023) 709–718. https://doi.org/10.12989/scs.2023.46.5.709.

[41] A.G. Yirik, S. Gündüz, D. Taştemür, M.A. Erden, Microstructural and mechanical properties of hot deformed AISI 4340 steel produced by powder metallurgy, Science of Sintering , 55 (2023) 45–56. https://doi.org/10.2298/SOS2301045Y.

[42] S. Xu, X. Sun, X. Liang, J. Liu, Q. Yong, Effect of hot rolling deformation on microstructure and mechanical properties of a high-ti wear-resistant steel, Jinshu Xuebao/Acta Metallurgica Sinica , 56 (2020) 1581–1591. https://doi.org/10.11900/0412.1961.2020.00124.

[43] I. Astm, Standard Test Method for Density, Oil content, and ınterconnected porosity of sintered metal structural parts and oil-ımpregnated bearings, B328-96 , 96 (2003) 1–4. https://scholar.google.com/scholar_lookup?title=Standard+Test+Method+for+Density,+Oil+Content,+and+Interconnected+Porosity+of+Sintered+Metal+Structural+Parts+and+Oil-Impregnated+Bearings&author=ASTM+B328-96&publication_year=2004 (accessed March 6, 2023).

[44] A. Kaynar, S. Gündüz, M. Türkmen, Investigation on the behaviour of medium carbon and vanadium microalloyed steels by hot forging test, Materials and Design , 51 (2013) 819–825. https://doi.org/10.1016/j.matdes.2013.04.102.

[45] S. Gündüz, A. Çapar, Influence of forging and cooling rate on microstructure and properties of

medium carbon microalloy forging steel, Journal of Materials Science , 41 (2006) 561–564. https://doi.org/10.1007/s10853-005-4239-y.

[46] S. Wang, L.G. Hou, J.R. Luo, J.S. Zhang, L.Z. Zhuang, Characterization of hot workability in AA 7050 aluminum alloy using activation energy and 3-D processing map, Journal of Materials Processing Technology , 225 (2015) 110–121. https://doi.org/10.1016/j.jmatprotec.2015.05.018.

[47] H. Inagaki, Role of annealıng twıns for graın refinement ın controlled rollıng of low carbon mıcroalloyed steel, Transactions of the Iron and Steel Institute of Japan , 23 (1983) 1059–1067. https://doi.org/10.2355/isijinternational1966.23.1059.

[48] H.S. I. Tamura, C. Ouchi, T. Tanaka, Thermomechanical Processing of High-Strength Low-Alloy Steels, 1988. https://doi.org/10.1016/c2013-0-04163-1.

[49] J.M. Chilton, M.J. Roberts, Microalloying effects in hot-Rolled low-Carbon steels finished at high temperatures, Metallurgical Transactions A , 11 (1980) 1711–1721. https://doi.org/10.1007/BF02660526.

[50] S.G. Hong, W.B. Lee, C.G. Park, Effects of tungsten addition on the microstructural stability of 9Cr-Mo steels, Journal of Nuclear Materials , 288 (2001) 202–207. https://doi.org/10.1016/S0022-3115(00)00558-4.

[51] A. Skowronek, D. Woźniak, A. Grajcar, Effect of mn addition on hot-working behavior and microstructure of hot-rolled medium Mn steels, Metals, 11 (2021) 1–14. https://doi.org/10.3390/met11020354.

[52] M. Korczynsky, Microalloying and thermo-mechanical treatment, In Proceedings of the International Symposium on Microstructure and Properties of HSLA Steels, Pittsburgh, PA, USA, 3 (1987) 169–201.

[53] S. Gunduz, M.A. Erden, H. Karabulut, M. Turkmen, The Effect of vanadium and titanium on mechanical properties of microalloyed PM steel, Powder Metallurgy and Metal Ceramics , 55 (2016) 277–287. https://doi.org/10.1007/s11106-016-9803-2.

[54] M.T. Erden, The effect of Ni on the microstructure and mechanical properties of Nb-V microalloyed steels produced by powder metallurgy, 2016. https://scholar.google.com/scholar?hl=ar&as_sdt=0%2C5&q=The+Effect+of+Ni+on+the+Microstructure+and+Mechanical+Properties+of+Nb-V+Microalloyed+Steels+Produced+by+Powder+Metallurgy&btnG= (accessed April 4, 2023).

[55] M.A. Erden, B. Ayvacı, The effect on mechanical properties of pressing technique in PM steels, Acta Physica Polonica A, 135 (2019) 1078–1080. https://doi.org/10.12693/APhysPolA.135.1078.

[56] K. Liu, H. Zhang, M. Xiu, Z. Huang, H. Huang, Y. Xu, R. Zhou, H. Xiao, Microstructure evolution, mechanical properties, and corrosion resistance of hot rolled and annealed Ti-Mo-Ni Alloy, Metals, 13 (2023) 566. https://doi.org/10.3390/met13030566.

[57] V.A. Tracey, Nickel sintered steels: Developments, status and prospects, in: Adv. Powder Metall., (1992) 303–314. https://doi.org/10.1016/0026-0800(92)90001-F.

[58] Fadaei, A. Nazari, M. Salari, T. Yildirim, Experimental investigation on the effect of the sintering temperature on the microstructure, hardness, and wear behavior of PM Cu-Fe alloys, Powder Metallurgy, 57 (2014) 213–222. https://doi.org/10.1179/1743290014Y.0000000047. https://doi.org/10.3390/met13020257.

[59] N. Alharthi, E.S.M. Sherif, H.S. Abdo, S.Z. El Abedin, Effect of nickel content on the corrosion resistance of ıron-nickel alloys in concentrated hydrochloric acid pickling solutions, Advances in Materials Science and Engineering, 2017 (2017). https://doi.org/10.1155/2017/1893672.

[60] C.A. Martins, G.L. de Faria, U. Mayo, N. Isasti, P. Uranga, J.M. Rodríguez-Ibabe, A.L. de Souza, J.A.C. Cohn, M.A. Rebellato, A.A. Gorni, Production of a non-stoichiometric Nb-Ti HSLA steel by thermomechanical processing on a steckel mill, Metals, 13 (2023). https://doi.org/10.3390/met13020405.

[61] S. Gündüz, M.A. Erden, H. Karabulut, M. Türkmen, Effect of the addition of niobium and aluminium on the microstructures and mechanical properties of micro-alloyed PM steels, Materiali in Tehnologije, 50 (2016) 641–648. https://doi.org/10.17222/mit.2015.248.

[62] A.G. Kostryzhev, A. Al Shahrani, C. Zhu, J.M. Cairney, S.P. Ringer, C.R. Killmore, E. V. Pereloma, Effect of niobium clustering and precipitation on strength of an NbTi-microalloyed ferritic steel, Materials Science and Engineering: A, 607 (2014) 226–235. https://doi.org/10.1016/j.msea.2014.03.140.

[63] A. Kammouni, W. Saikaly, M. Dumont, C. Marteau, S. Lacroix, E. Stenback-Lund, F. Oudrhiri Hassani, A. Perlade, Microstructural characterization and mechanical properties of vanadium microalloyed steels, Journal of Materials and Environmental Science, 6 (2015) 3457–3464.

[64] G. Xu, X. Gan, G. Ma, F. Luo, H. Zou, The development of Ti-alloyed high strength microalloy steel, Materials and Design, 31 (2010) 2891–2896. https://doi.org/10.1016/j.matdes.2009.12.032.

[65] N. Saleh, S. Mansour, R. Hague, Investigation into the mechanical properties of rapid manufacturing materials, Solid Freeform Fabrication Symposium Proceedings (2002) 287–296. http://mit.imt.si/izvodi/mit112/chokkalingam.pdf (accessed March 1, 2024).

[66] M.A. Erden, The effect of the sintering temperature and addition of niobium and vanadium on the microstructure and mechanical properties of microalloyed PM steels, Metals, 7 (2017) 329. https://doi.org/10.3390/met7090329.

[67] M.A. Erden, The effect of sıntering tıme on tensıle strength of nb-v mıcroalloyed powder metallurgy steels, NWSA Academic Journals, 15 (2020) 15–22. https://doi.org/10.12739/nwsa.2020.15.1.2a0180.

[68] D. Taştemür, S. Gündüz, D. Tastemur, S. Gunduz, M.A. Erden, Investigation of thermomechanical processing of Nb microalloyed steel produced by powder metallurgy, Gazı Unıversıty Journal of Scıence, 35 (2021) 606–616. https://doi.org/10.35378/gujs.835371.

[69] M.A. Erden, F. Aydın, Wear and mechanical properties of carburized AISI 8620 steel produced by powder metallurgy, International Journal of Minerals, Metallurgy and Materials, 28 (2021) 430–439. https://link.springer.com/article/10.1007/s12613-020-2046-8 (accessed March 5, 2023).

[70] G. Zhou, W. Wei, Q. Liu, Effect of hot rolling on microstructural evolution and wear behaviors of G20CrNi2 MoA bearing steel, Metals, 11 (2021) 957. https://doi.org/10.3390/met11060957.

[71] A. Günen, K.M. Döleker, M.E. Korkmaz, M.S. Gök, A. Erdogan, Characteristics, high temperature wear and oxidation behavior of boride layer grown on Nimonic 80A Ni-based superalloy, Surface and Coatings Technology, 409 (2021) 126906. https://doi.org/10.1016/j.surfcoat.2021.126906.

[72] M.K. Gupta, M.E. Korkmaz, C.S. Shibi, N.S. Ross, G. Singh, R. Demirsöz, M. Jamil, G.M. Królczyk, Tribological characteristics of additively manufactured 316 stainless steel against 100 Cr6 alloy using deep learning, Tribology International, 188 (2023) 108893. https://doi.org/10.1016/j.triboint.2023.108893.

[73] M.K. Gupta, R. Demirsöz, M.E. Korkmaz, N.S. Ross, Wear and friction mechanism of

stainless steel 420 Under various lubrication conditions: a tribological assessment with ball on flat test, Journal of Tribology, 145 (2023). https://doi.org/10.1115/1.4056423.

[74] M.E. Korkmaz, M.K. Gupta, G. Singh, M. Kuntoğlu, A. Patange, R. Demirsoz, N.S. Ross, B. Prasad, Machine learning models for online detection of wear and friction behaviour of biomedical graded stainless steel 316L under lubricating conditions, International Journal of Advanced Manufacturing Technology, 128 (2023) 2671–2688. https://doi.org/10.1007/s00170-023-12108-3.

[75] S. Polat, Y. Sun, E. Çevik, H. Colijn, M.E. Turan, Investigation of wear and corrosion behavior of graphene nanoplatelet-coated B4C reinforced Al–Si matrix semi-ceramic hybrid composites, Journal of Composite Materials, 53 (2019) 3549–3565. https://doi.org/10.1177/0021998319842297.

[76] F. Gao, Y. Hu, Z. Gong, T. Liu, T. Gong, S. Liu, C. Zhang, L. Quan, B. Kaveendran, C. Pan, Fabrication of chitosan/heparinized graphene oxide multilayer coating to improve corrosion resistance and biocompatibility of magnesium alloys, Materials Science and Engineering C, 104 (2019) 109947. https://doi.org/10.1016/j.msec.2019.109947.

[77] T. Meesak, C. Thedsuwan, Corrosion behaviours of stainless steel parts formed by powder metallurgy process, in: Mater. Today Proc., Elsevier, 2018: pp. 9560–9568. https://doi.org/10.1016/j.matpr.2017.10.138.

[78] Y.S. Kim, J.G. Kim, Corrosion behavior of pipeline carbon steel under different iron oxide deposits in the district heating system, Metals, 7 (2017) 182. https://doi.org/10.3390/met7050182.

[79] H. Simsir, M.A. Erden, Investigation of the mechanical, tribological, and corrosion properties of 316L SS-HTC composites, Canadian Metallurgical Quarterly (2023). https://doi.org/10.1080/00084433.2023.2247176.

LIST OF FIGURES

LIST OF TABLES